Low-coordination transition metal sites on oxygen vacancy enriched strontium titanate-based perovskites enable highly selective photocatalytic CO_2 reduction to CH_4

Yibo Gao [a], Miaomiao Zhang [a], Yang Jin [a], Meng Zhou [a], Yanpeng Mao [a,*], Jian Sun [b], Wenlong Wang [a], Zhanlong Song [a]

[a] National Engineering Laboratory for Reducing Emissions from Coal Combustion, Engineering Research Center of Environmental Thermal Technology of Ministry of Education, Shandong Key Laboratory of Energy Carbon Reduction and Resource Utilization, School of Energy and Power Engineering, Shandong University, Jinan, Shandong 250061, China
[b] Dalian National Laboratory for Clean Energy, Dalian Institute of Chemical Physics, Chinese Academy of Sciences, 116023 Dalian, China

ABSTRACT

The photochemical conversion of CO_2 into high-value single hydrocarbon fuels such as CH_4 remains a challenge. Here we have prepared a series of perovskites V_O-SrTiMO$_3$ (M = Mn, Fe, Co) with rich oxygen vacancies. Among them, Mn-doped perovskite (V_O-STMn$_{0.2}$) exhibited 18.21 μmol g^{-1} yield and nearly 100 % selectivity for CH_4, as well as excellent reproducibility of about 15 h. Through a combination of advanced characterization and theoretical calculations, we found that the low-coordination transition metal site was able to stabilize the critical COOH* and CO* intermediates, thereby altering the reaction pathway to form CH_4 instead of CO. Most importantly, this work demonstrated that the relative center between the 2p orbitals of the oxygen atom of the CO_2 reduction intermediate and the 3d orbitals of the low-coordination metal site regulates the reaction mechanism of CO_2 reduction, offering the possibility of achieving efficient photochemical reduction of CO_2.

1. Introduction

The direct use of solar energy to boost carbon recovery and convert CO_2 into hydrocarbon fuels is undoubtedly a promising strategy for mitigating the greenhouse effect and securing future energy supplies [1]. Unfortunately, photoreduction of the extremely stable CO_2 molecule is very difficult and elaborate owing to the high C═O dissociation energy of about 750 kJ mol^{-1} [2]. Moreover, due to the complex electron and proton transfer processes involved, a wide variety of products such as CO, CH_3OH and CH_4 can be produced in the CO_2 photoreduction process. Therefore, it remains a major challenge to design highly active photocatalytic systems with a highly pure gaseous product.

In recent years, researchers have tried to improve the light absorption and CO_2 adsorption/activation of photocatalysts by introducing foreign elements [3], co-catalysts loaded with noble metals [4], surface defects [5] and functional groups [6,7]. For perovskite oxides (ABO$_3$), metal cation doping involves substitution of A or B sites, and the d-type orbitals of the doped metal cations will overlap and hybridize with those of the existing A/B site metals, and exhibit d-d transition sub-peak

absorption in the low photon energy region [8,9], which can dramatically alter the band structure and create new activity for photocatalytic CO_2 reduction [10]. SrTiO$_3$ is an archetypal perovskite oxide, however, it is not a good candidate for a photocatalyst since it is only active under ultraviolet radiation [11]. Many studies have investigated the introduction of various dopants such as Cr [12], Co [13], Rh [14], Al [15] and Bi [16] to extend the light absorption of SrTiO$_3$ into the visible range. In addition, the introduction of oxygen vacancies into perovskite oxides is also an effective approach to modify their photocatalytic performance [17]. Oxygen vacancies can reduce the coordination numbers of the neighboring metal atoms to provide more active sites for the intermediates [18,19], thus further optimizing energetics of the catalytic reaction [20,21]. In photocatalysis, low-valence electron-rich 3d transition metal ions with specific electronic structures (such as Ti^{3+} (III) [22], Mn^{3+} (III) [23], Ni$^+$ (I) [24], and Cu$^{\delta+}$ (δ < 2) [25]) can act as catalytic centers or promoters to enhance the kinetics of a variety of thermodynamically unfavorable reactions. [26] Advanced structural and theoretical analyses attribute the excellent activity to Jahn-Teller distortion, large amounts of oxygen vacancies around the doped

---

* Corresponding author.
E-mail address: maoyanpeng@sdu.edu.cn (Y. Mao).

transition metal ions and the introduction of compressive strain into the host. This synergistic effect promotes molecular adsorption and activation, and rapid charge separation [27]. Although numerous theoretical and experimental investigations have been carried out on the surface defects of perovskite oxides [28], detailed studies on the optimization of the chemical absorption behavior of intermediates in the CO_2 reduction process are still lacking.

Herein, based on defect chemistry theory, we constructed oxygen vacancy enriched perovskites $SrTiMO_3$ (M = Mn, Fe, Co) for CO_2 photoreduction. Detailed characterization shows that the introduction of oxygen vacancies creates an abundance of low-coordination transition metal sites, which significantly improves the separation and transfer efficiency of carriers. In situ diffuse reflectance infrared Fourier transform spectroscopy (DRIFTS) and density functional theory (DFT) calculations confirm that the low-coordination transition metal sites can lower the energy barrier from CO* to CHO*. Meanwhile, the relative center between the 2p orbitals of the oxygen atom of the CO_2 reduction intermediate and the 3d orbitals of the low coordination metal site regulates the adsorption stability of the low coordination metal site to the oxygen intermediate, ultimately conferring the selectivity for desired CH_4 product.

2. Experimental

2.1. Chemicals and materials

Strontium nitrate ($Sr(NO_3)_2$, AR, Sinopharm Chemical Reagent), manganese chloride tetrahydrate ($MnCl_2 \cdot 4 H_2O$, 99.99 %, Macklin), iron nitrate nonahydrate ($Fe(NO_3)_3 \cdot 9 H_2O$, 99.99 %, Macklin), cobalt nitrate hexahydrate ($Co(NO_3)_2 \cdot 6 H_2O$, 99.99 %, Macklin), tetrabutyl titanate ($C_{16}H_{36}O_4Ti$, AR, Macklin), ethanolamine (EA, AR, Macklin), sodium hydroxide (NaOH, 95 %, Sinopharm Chemical Reagent), Sodium borohydride ($NaBH_4$, AR, Sinopharm Chemical Reagent). All the chemicals were used directly without any further purification.

2.2. Synthesis of $SrTiO_3$ and $SrTi_{1-x}M_xO_3$ perovskite oxides

The pure-$SrTiO_3$ and $SrTi_{1-x}M_xO_3$ (M = Mn, Fe, Co) were synthesized by a facile one-pot solvothermal method [29]. In a typical procedure, 8 mmol of tetrabutyl titanate and 2 mmol $MnCl_2 \cdot 4 H_2O$ were dissolved in 20 mL of EA and stirred for 30 min 50 mL of 3 M NaOH aqueous solution was added to the solution and stirred for a further 30 min to obtain the precipitate suspension. 10 mL of aqueous solution containing 10 mmol of $Sr(NO_3)_2$ was added into the suspension and the solution stirred for 30 min. The solution was then transferred into a 100 mL Tefon-lined autoclave, sealed, and heated at 180 °C for 24 h, and allowed to cool to room temperature naturally. The final product was collected by centrifuging the mixture, washed with ethanol and deionized water many times until the organic residuals were completely removed, and then dried in vacuum at 80 °C for 10 h. The obtained $STMn_{0.2}$ perovskite oxides were calcined at 350 °C for 2 h in static air and then cooled to room temperature for further characterization. By tuning the molar ratio of tetrabutyl titanate and transition metal ion precursor chemicals in the final suspension solution, the obtained $SrTi_{1-x}M_xO_3$ samples were designed as STM_x (x = 0.1, 0.2, 0.3, 0.4), and the pure-$SrTiO_3$ sample was termed STO.

2.3. Synthesis of oxygen vacancy enriched $SrTiO_3$ and $SrTi_{1-x}M_xO_3$ perovskite oxides

In a typical procedure, the obtained $SrTiO_3$ ($SrTi_{1-x}M_xO_3$) perovskite oxide was completely ground with $NaBH_4$ (with a mass ratio of 1:1) and the mixture was then placed in a porcelain crucible. It was further calcined at 350 °C for 2 h in Ar (99.999 %) at a ramp rate of 2.5 °C min^{-1}, and allowed to cool to room temperature. Finally, the resulting powders were washed with ethanol and deionized water many times

until the organic residuals were completely removed, and then dried in vacuum at 80 °C for 10 h. The obtained powder was designed as V_O-STO (V_O-STM_x) and collected for further characterization.

Additional experimental details including materials, characterization, parameters for DFT calculations, and the photocatalytic test process can be found in the Supplementary Material.

3. Results and discussion

3.1. Structural and electronic states

As is displayed in Fig. 1a and Fig. S1, the XRD patterns indicate that the transition metal ions M can be successfully doped into the perovskite STO lattice (PDF#84-0444) within the doping ratio range of 0.1–0.3. However, when the doping ratio is 0.4, the XRD pattern displays obvious impurity peaks at 40–50° (marked with *), which can be indexed to $SrCO_3$ (PDF#05-0418). Therefore, only the STM_x catalysts with M-doping ratio from 0.1 to 0.3 were investigated. For $STM_{0.3}$, the peaks were slightly shifted to higher angles compared to $STM_{0.1}$, indicating lattice shrinkage due to partial replacement of the larger Ti^{4+} ion (0.745 Å) by the smaller Mn^{3+}/Mn^{4+} (0.72/0.67 Å), Fe^{3+} (0.69 Å) or Co^{3+} (0.685 Å) ions [30]. Notably, $STMn_{0.2}$ showed the same degree of peak shift as $STMn_{0.3}$. The Rietveld refinement method was used to fit the XRD results to obtain more detailed crystal structure information (Fig. S2). The refinement results reveal that perovskites STO, $STMn_{0.1}$, $STMn_{0.2}$ and $STMn_{0.3}$ have the same structure of Pm-3m, and the unit cell volume decreases from 59.456 to 58.533 $Å^3$ after doping with Mn ions. The SEM results show that the average particle size of STO is around 140 nm (Fig. 1b). Following Mn ion doping, the average particle size of the $STMn_x$ gradually decreases (Fig. 1c-e).

The density of states (DOS) of STO before and after the substitution of the transition metal ion was further investigated. As shown in Fig. 1f, the valence band (VB) of STO mainly consisted of O 2p orbitals and the conduction band (CB) primarily of Ti 3d states. The band gap of STO is about 2.4 eV, smaller than the experimental value because of the limitations of PBE method. After doping with M ions, the STM can be observed with a new energy level consisting mainly of M 3d and O 2p, resulting in a narrower band gap. For the $STMn_x$, the new energy level as shallow donor energy levels near the bottom of the CB can absorb additional long wavelength visible light. The new energy levels of STFe and STCo as shallow acceptor energy levels near the top of the VB may also lead to an extension of the light absorption range. In conclusion, these impurity states can prolong the lifetime of the photogenerated carriers, thereby increasing the efficiency of the reaction.

After reduction with $NaBH_4$, XPS spectroscopy was carried out on the V_O-$STMn_x$ to determine its electronic states. Fig. 2a shows the O 1 s spectra, which can be deconvoluted into peaks corresponding to the various oxygen species including lattice oxygen (O_{lat}, 529.3–530.5 eV), vacancy oxygen (O_v, 530.5–531.7 eV) and surface-adsorbed oxygen (O_{ads}, 531.8–532.8 eV), respectively [31,32]. Compared to V_O-$STMn_{0.1}$, the binding energy of O 1 s of V_O-$STMn_{0.2}$ shifts into the higher energy region by ~0.6 eV. The fitting results of O 1 s spectra confirm that V_O-$STMn_{0.2}$ (26.1 %) has a higher content of oxygen vacancies than V_O-$STMn_{0.1}$ (17.5 %) and V_O-$STMn_{0.3}$ (19.2 %). The Mn 2p spectrum shows two peaks at 653 and 643 eV (Fig. 2b), which belongs to Mn 2p3/2 and Mn 2p1/2, respectively. The peaks at 646 eV correspond to the Mn^{2+} satellite feature [28]. For V_O-$STM_{0.2}$, it exhibits a significantly greater proportion of the peaks at 646 eV than that of V_O-$STMn_{0.1}$/V_O-$STMn_{0.3}$ (16.1 % vs 15.3/15.6 %), evidencing more abundant Mn^{n+} species in V_O-$STM_{0.2}$. Compared to $STMn_{0.2}$, there is an imperceptible shift in the binding energy of Sr 3d and Ti 2p in V_O-$STM_{0.2}$ (Fig. S3). In addition, the Ti 2p peak of V_O-$STMn_{0.2}$ with Gaussian distribution determines the existence of Ti^{4+}, while the percentage of Ti^{3+} hardly changes.

The XRD pattern of V_O-$STMn_{0.2}$ also possesses a similar cubic shape (Fig. S4), while its unit cell volume is enlarged to 59.249 $Å^3$ compared to
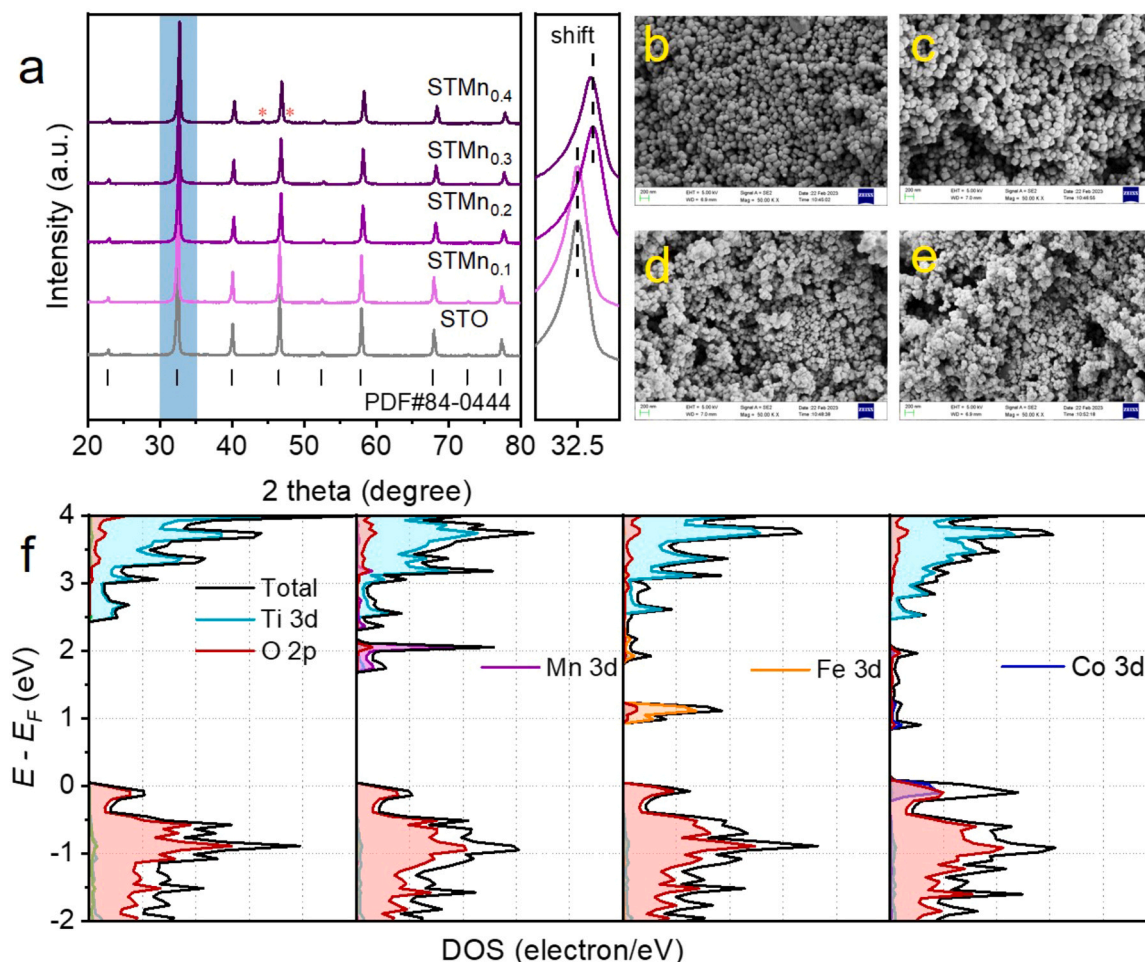
Fig. 1. (a) XRD patterns of perovskites STMn$_x$ (x = 0.1–0.4). SEM image of (b) STO, (c) STMn$_{0.1}$, (d) STMn$_{0.2}$, and (e) STMn$_{0.3}$. (f) The density of states of STO and STM (M = Mn, Fe, Co).

that of STMn$_{0.2}$. As displayed in the TEM images of V_O-STMn$_{0.2}$ and STMn$_{0.2}$ in Fig. 2c and Fig. S5, both samples have a well crystallized structure with an average particle size of 93.93 nm for V_O-STMn$_{0.2}$ and 88.36 nm for STMn$_{0.2}$. Moreover, the HRTEM image in Fig. 2d shows two interplanar spacing values of 0.278 nm and 0.389 nm with an angle of 45°, attributed to the (110) and (100) facets of V_O-STMn$_{0.2}$, respectively. Accordingly, it could be concluded that the exposed surface consists of (001) facets of V_O-STMn$_{0.2}$. Meanwhile, it is worth remarking that the significant stacking defect can be observed in Fig. 2d (as indicated by the white dash), which is caused by the narrowing of the lattice spacing after Mn ion substitution. The corresponding elemental mapping in Fig. 2e-i confirms the homogeneous distribution of Sr, Ti, Mn and O elements, and the elemental ratio is approximately Sr:Ti:Mn = 1:0.79:0.17 based on energy dispersive spectroscopy (Fig. S6).

The structural information and oxidation state of the catalysts are revealed by Raman spectroscopy. As show in Fig. 2j, STMn$_{0.2}$ displays the typical TO$_4$ and LO$_4$ peaks at 525 cm^{-1} and 750 cm^{-1}, respectively [33]. In contrast, V_O-STMn$_{0.2}$ shows a blueshift of the TO$_4$ and LO$_4$ peaks, indicating mass fluctuation at the oxygen position, which may be caused by the presence of oxygen vacancies. To provide more convincing information, electron spin resonance (ESR) spectroscopy was used to characterize the local environment of the present samples (Fig. 2k). The STMn$_{0.2}$ displays a symmetrical ESR signal at g = 1.997, which is usually associated with the characteristics of Mn^{4+} ions.[34] After reduction, the V_O-STMn$_{0.2}$ signal becomes stronger, indicating that more Mn ions are exposed due to the increased surface oxygen vacancies [35,36]. The ESR spectrum of V_O-STMn$_{0.2}$ at 100 K was further

measured. As seen in Fig. 2j, V_O-STMn$_{0.2}$ has a single sextet of lines with a hyperfine splitting of 78 Oe, which is indicative of Mn^{4+} ions doped at the Ti site in STO. Notably, in addition to the Mn^{4+} spectrum, a spectrum associated with Mn^{2+} appears with hyperfine splitting to 86 Oe. This obviously indicates that electrons supplied by oxygen vacancies are effectively trapped by the Mn^{4+} sites, converting Mn^{4+} to Mn^{2+} and maintaining the insulation of the sample [37].

It is reasonable to conclude that oxygen vacancies in perovskite STMn$_{0.2}$ tend to be created in the MnO$_6$ octahedra rather than the TiO$_6$ octahedra. DFT computations were performed to further determine the oxygen vacancy formation energies (E$_f$) of STMn$_x$ on the MnO$_6$ octahedron and TiO$_6$ octahedron. The E$_f$ is evaluated according to the following Eq. (1):

$$E_f = E_*^{V_O} + 1/2E_{O_2} - E_* \tag{1}$$

in which $E_*^{V_O}$ is the total energy of the substrate structure with oxygen vacancy, E_* denotes the total energy of the substrate structure without oxygen vacancy, and E_{O_2} is the energy obtained from O$_2$ molecule. As illustrated in Fig. 2l, the E$_f$ values are 3.66 eV (V$_{O-Mn}$) for the MnO$_6$ octahedron and 4.45 eV (V$_{O-Ti-1}$) or 4.37 eV (V$_{O-Ti-2}$) for the TiO$_6$ octahedron, suggesting that oxygen vacancies are more favorably generated in the MnO$_6$ octahedron. Bader charge and differential charge density analysis was performed to study the charge redistribution and trapping (Fig. 2m). The creation of oxygen vacancies redistributes the charges on the surface as well as the layer beneath the surface of STMn$_x$, while the Mn atoms in the center of the MnO$_6$ octahedron are allocated more electrons (+1.61e → +1.16e) than the Sr (+1.57e → +1.52e) atoms on
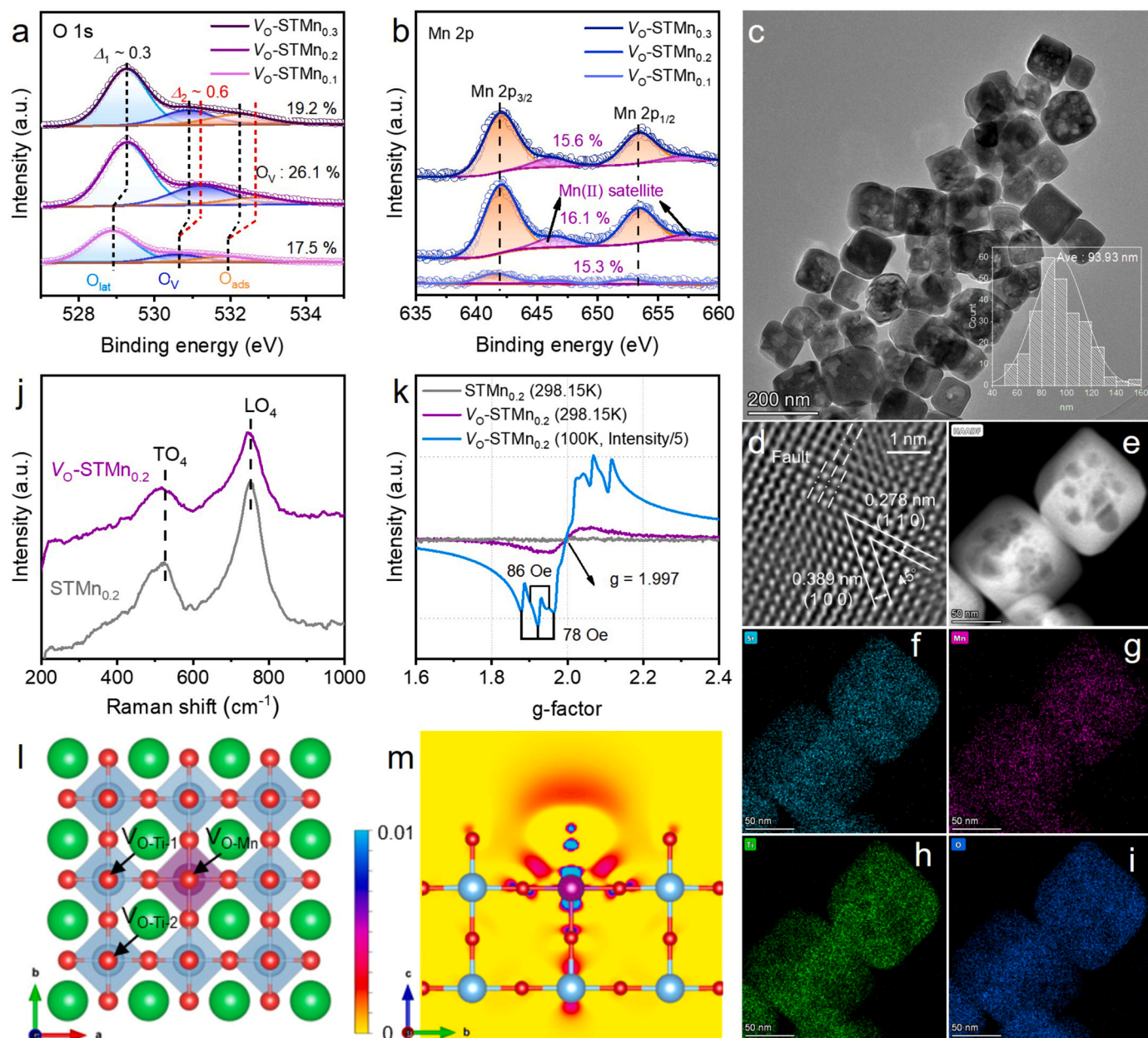
Fig. 2. The XPS spectra of (a) O 1s and (b) Mn 2p for V_O-STMn$_x$. (c) TEM image of V_O-STMn$_{0.2}$, the inset shows the particle size distribution with an average size of 93.93 nm. (d) HRTEM image of V_O-STMn$_{0.2}$. (e-i) EDS elemental mappings of Sr (cyan), Mn (purple), Ti (green) and O (blue) with scale bars of 50 nm. (j) Raman shifts. (k) ESR spectra, in which the signal at g = 1.997 corresponds to the Mn^{4+} ions. (l) View of the positions of oxygen vacancy in STMn$_x$. (m) 2D charge density differences. The charge density of blue represents electron accumulation, and yellow denotes electron depletion (e bohr^{-3}). The atomic color codes: green (Sr), cyan (Ti), purple (Mn), and red (O) balls, respectively.

the surface. Notably, these charge-enriched Mn sites may serve as highly active sites for strongly trapping C or O atoms into stable intermediate configurations, offering the possibility of selectively tailoring product.

XAS spectroscopy measurements at the Mn K-edges were carried out to assess the chemical environment of V_O-STMn$_{0.2}$ and STMn$_{0.2}$. As presented in Figs. 3a and 3b, the normalized X-ray absorption near edge structure (XANES) spectra on the V_O-STMn$_{0.2}$ and its corresponding first derivative are obviously shifted to a lower energy direction compared with that of STMn$_{0.2}$, manifesting the lower average Mn valence state. Based on the linear relationship between the peak positions of the first derivatives of the Mn XANES spectra and the oxidation states, we calculated the valance states of the Mn atoms (Fig. 3c) [38]. The V_O-STMn$_{0.2}$ shows the lower Mn valance states (2.4 +) than the STMn$_{0.2}$ (3.2 +), which is in accordance well with the XPS data. The extended

X-ray absorption fine structure (EXAFS) spectra provided further structural information (Fig. 3d). The peak between 1.0 and 2.0 Å in the R-space represents the Mn-O shell. However, the intensity of the peak for V_O-STMn$_{0.2}$ is weaker than that for the STMn$_{0.2}$, confirming the reduced Mn-O coordination number (Fig. S7). Furthermore, least squares curve parameter fitting was performed to analyze the quantitative coordination numbers of Mn confined in the V_O-STMn$_{0.2}$ and STMn$_{0.2}$. The results of the EXAFS data fitting analysis are summarized in Fig. S8 and Table S1. The coordination number for Mn-O decreased from 5.65 to 4.41 after reduction with NaBH$_4$, which is attributed to the loss of lattice oxygen atoms. The corresponding EXAFS wavelet transform (WT) analysis results are shown in Fig. 3e-h. A smaller intensity maximum at about 4 Å^{-1} is observed, which correlates with the Mn-O pathway in V_O-STMn$_{0.2}$, illustrating the low Mn-O coordination configuration. It is
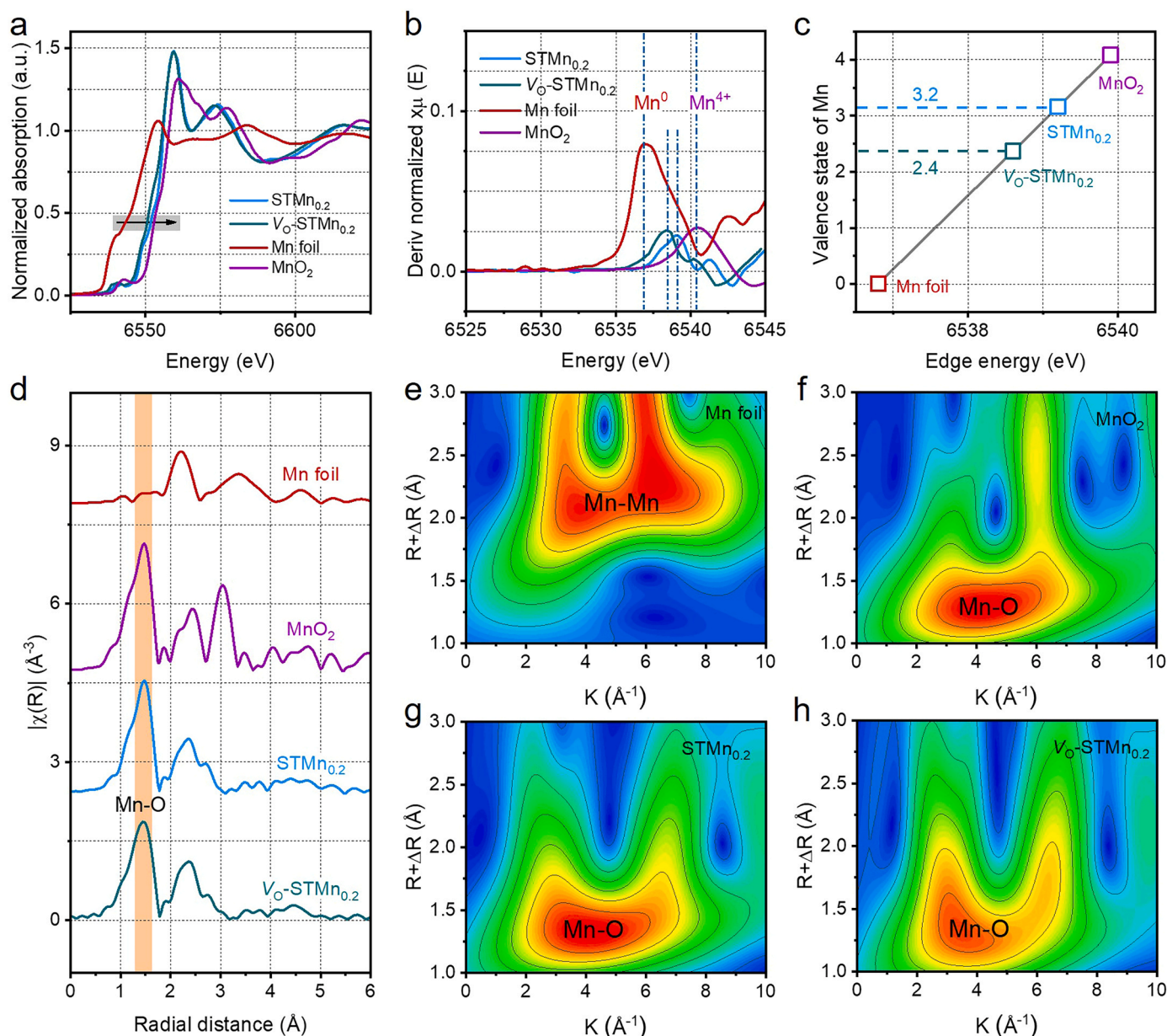
Fig. 3. (a) Mn K-edge XANES spectra. (b) The first derivation of Mn K-edge XANES. (c) Mn oxidation state. (d) FT k^2-weighted EXAFS spectra of STMn$_{0.2}$, V_O-STMn$_{0.2}$, and standard samples. (e-h) WT analysis at the Mn K edge of different samples.

concluded that the lower coordination environment effectively regulates the electron state, and the altered e_g electron occupancy of Mn site can provide high active sites for catalytic reactions [19].

3.2. Photocatalytic performance for CO$_2$ reduction

As a precondition for photocatalytic CO$_2$ reduction, the adsorption and activation of CO$_2$ and H$_2$O on STMn$_{0.2}$ and V_O-STMn$_{0.2}$ surfaces in dark condition was studied using in situ DRIFTS. As depicted in Fig. 4a, exposure of V_O-STMn$_{0.2}$ to the H$_2$O/CO$_2$ atmosphere in the dark can induce the formation of highly adsorbed H$_2$O* (1635 cm^{-1}) and carbonate or bicarbonate species (monodentate (m-CO$_3^{2-}$) at 1302, 1458, 1508, 1540, 1560 and 1577 cm^{-1}, bidentate (b-CO$_3^{2-}$) at 1338, 1363, 1375, 1603 and 1650 cm^{-1}, and bicarbonate (HCO$_3$) at 1395, 1420, 1436, 1474 and 1685 cm^{-1}) [39,40]. In particular, the key precursors of CO$_2$* species are observed at 1670 and 1700 cm^{-1}, indicating that the single-electron reduction of CO$_2$ to CO$_2$* can readily occur on the defective surface of V_O-STMn$_{0.2}$. Albeit of similar carbon active species

observed for STMn$_{0.2}$, the detected absorption peaks of these intermediates are significantly lower than those of V_O-STMn$_{0.2}$ in the initial 0–30 min of CO$_2$ adsorption (Fig. 4b). For example, STMn$_{0.2}$ produces dominant m-CO$_3^{2-}$ instead of b-CO$_3^{2-}$, while the latter was the more robust site required for CO$_2$ adsorption [18]. This is further supported by temperature programmed desorption (TPD) measurements of CO$_2$. Fig. S9 shows the CO$_2$-TPD curves of STMn$_{0.2}$ and V_O-STMn$_{0.2}$, with the amount of CO$_2$ adsorbed derived from the combined area of the curves. Clearly, V_O-STMn$_{0.2}$ has a higher adsorption capacity compared to STMn$_{0.2}$, indicating that V_O-STMn$_{0.2}$ has more CO$_2$ adsorption and activation sites. As a result, the abundance of rationally created surface oxygen vacancies provides more adsorption sites and enhances the reactivity of V_O-STMn$_{0.2}$.

To better understand the adsorption and activation of CO$_2$ on the surface with oxygen vacancies, DFT calculations were conducted to compare the CO$_2$ adsorption over the oxygen vacancy and the perfect STMn$_x$ surface. The adsorption energy ($E_{ads} = \Delta G_{CO_2^*}$) of CO$_2$ adsorption over the V_O-STMn$_x$ (−1.86 eV) is higher than that of CO$_2$ adsorption on
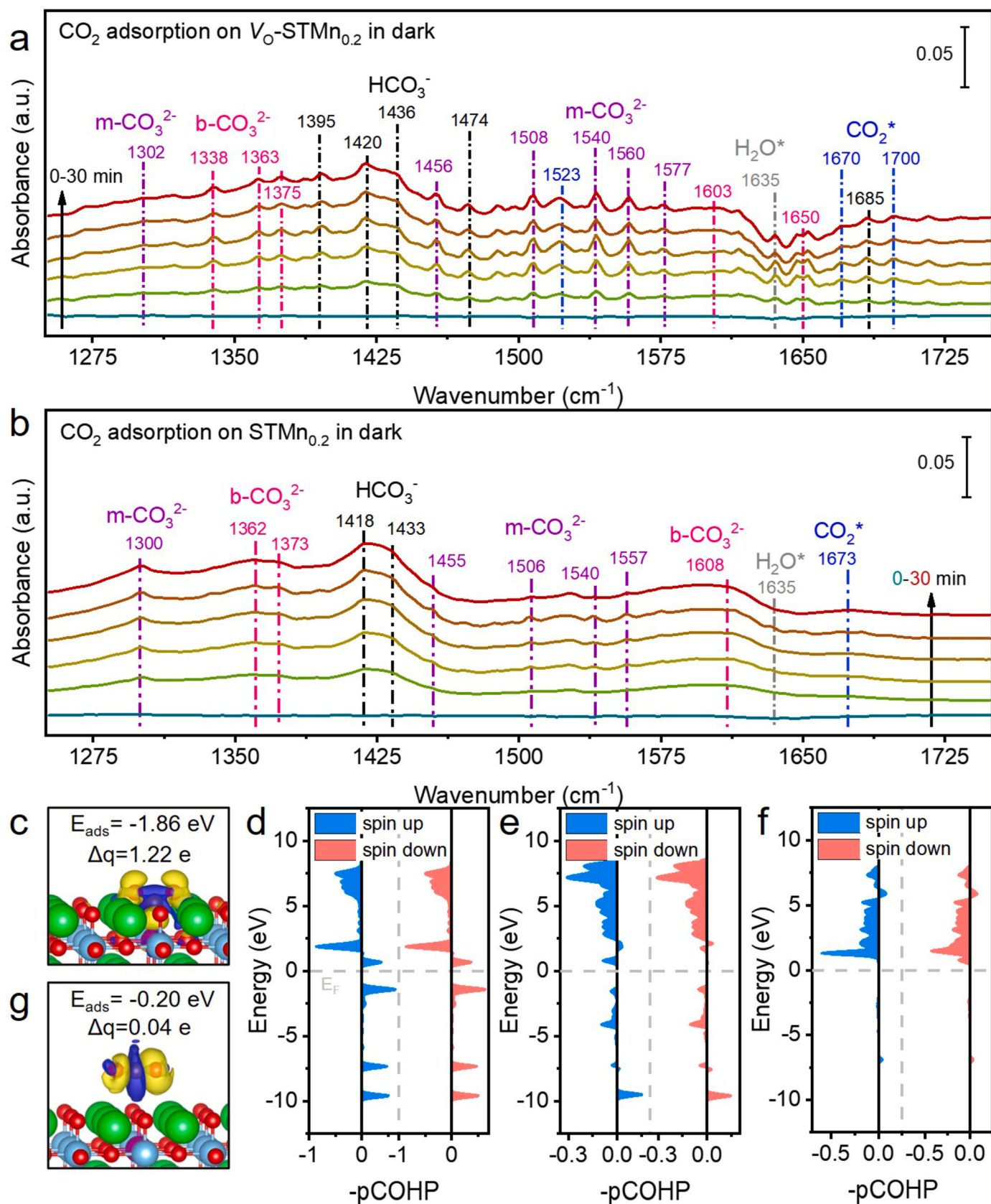
Fig. 4. In situ DRIFTS test for CO_2 and H_2O interaction with (a) V_O-STMn$_{0.2}$ and (b) STMn$_{0.2}$ in dark. Charge difference distributions for (c) V_O-STMn$_x$ and (g) STMn$_x$ following CO_2 adsorption (charge accumulation is in yellow and depletion in blue, positive values for Δq indicate electron accumulation on CO_2, and E$_{ads}$ is CO_2 adsorption energy on surface). Isosurfaces are 0.002 e bohr^{-3}. Strontium, titanium, manganese, and oxygen atoms are denoted as green, cyan, purple, and red balls, respectively. (d) pCOHP between carbon atom in CO_2 and Mn active site on V_O-STMn$_x$. pCOHP between oxygen atom in CO_2 and surface Sr atom on (e) V_O-STMn$_x$ and (f) STMn$_x$.

STMn$_x$ (-0.20 eV). The bond situation of CO_2 adsorbed in two different surfaces was then further compared by the charge difference and Bader charge analysis. As seen in Fig. 4c, the C atom is bound with the unsaturated Mn sites in V_O-STMn$_x$, causing the O=C=O bond to bend (122°) and elongate (1.28 Å). The strong electron scale is distributed within the valence bonds, indicating the formation of a firm chemical bond between C atom and Mn site. The feedback π electrons from the Mn d orbital were transferred to the vacant orbital of C, resulting in an increase in the charge density of the C atom. The correlation results were confirmed by the Bader charge, where electrons (1.22 e) were

transferred from the surface to the CO_2 molecule. The above results were further supported by the calculation of the projected Crystal Orbital Hamilton Population (pCOHP) adsorbed by CO_2 on V_O-STMn$_x$ and STMn$_x$. In Fig. 4d, it is seen that most of the bonding orbitals of the C atom of CO_2 and the Mn site are in the valence band below the Fermi level (E_F), while the anti-bonding orbitals are mainly distributed in the conduction band above the E_F. In contrast, there are many anti-bonding orbitals below the E_F for O atom of CO_2 and the surface Sr atom (Fig. 4e). Integral crystal orbital Hamiltonian (ICOHP) results show that the interaction between C atom and Mn active site is stronger than that
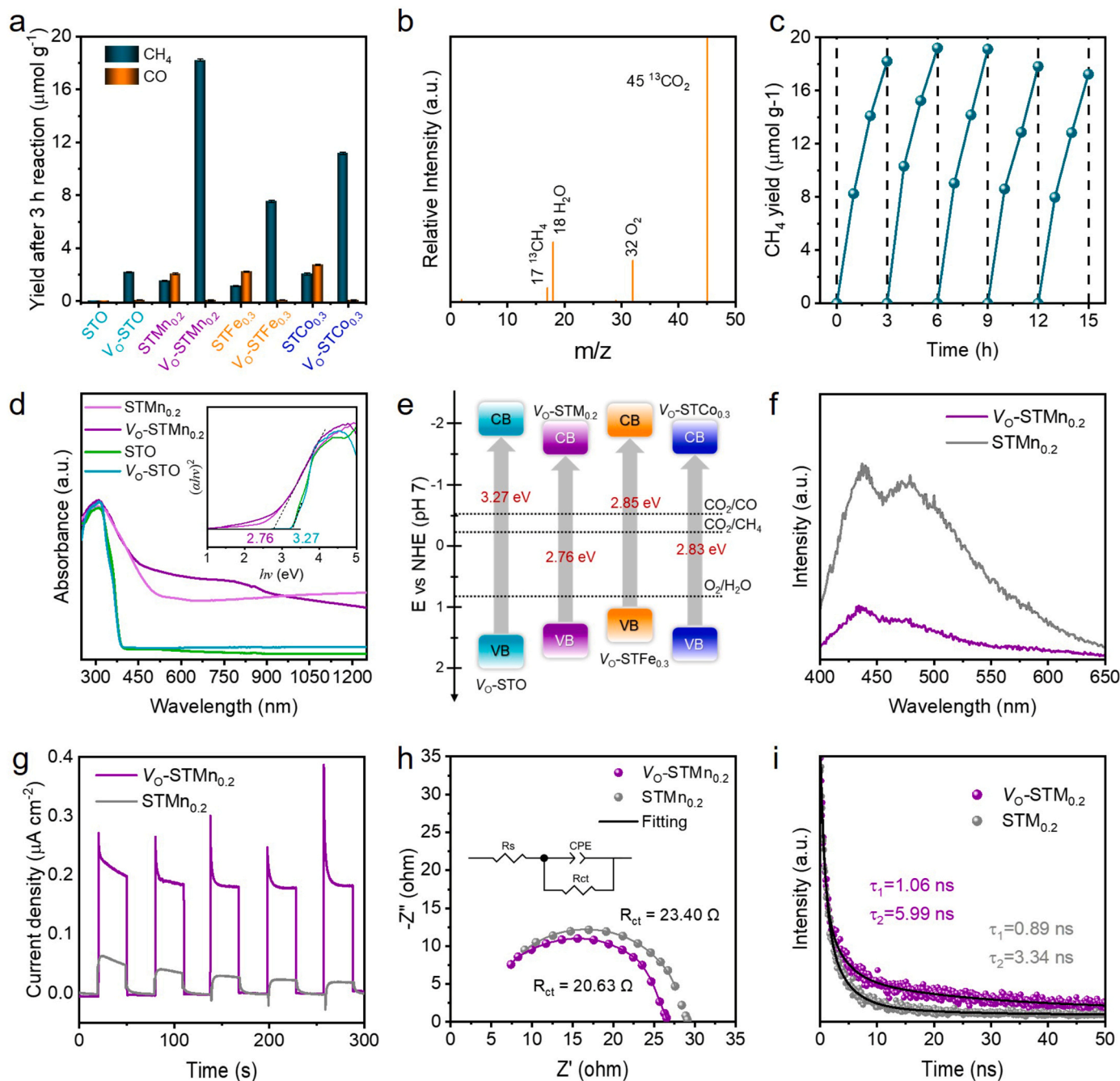

Fig. 5. (a) Production rates of CH$_4$ (green columns) and CO (yellow columns) of CO_2 photoreduction over STO, V_O-STO, STM$_x$ and V_O-STM$_x$ under Xenon lamp illumination. (b) Mass spectra of $^{13}CH_4$ (m/z = 17) and ^{13}CO (m/z = 29) produced in the photocatalytic reduction of $^{13}CO_2$ over V_O-STMn$_{0.2}$. (c) Cycling measurements of CO_2 photoreduction to CH$_4$ for the V_O-STMn$_{0.2}$ perovskite. (d) UV–vis diffuse reflectance spectra and inset for bandgap. (e) Schematic diagram of electronic band structures; the arrows represent the electron leap from the valence band (VB) to the conduction band (CB). (f) PL spectra for V_O-STMn$_{0.2}$ and STMn$_{0.2}$. (g) Transient photocurrent density for V_O-STMn$_{0.2}$ and STMn$_{0.2}$ in 0.1 M Na$_2$SO$_4$ aqueous solution. (h) EIS spectra for V_O-STMn$_{0.2}$ and STMn$_{0.2}$. Inset is the fitted circuit. (i) TSPL spectra for V_O-STMn$_{0.2}$ and STMn$_{0.2}$.

between O atom and surface Sr site (-ICOHP=2.34 for C-Mn vs -ICOHP=1.43 for O-Sr) [41]. Additionally, the weak interaction between CO_2 and the $STMn_x$ surface was also confirmed (-ICOHP=1.62 of O-Sr) and few electrons (0.04 e) transferred from the surface to the CO_2 molecule (Figs. 4f and 4g). In conclusion, these experimental and computational results demonstrate the stronger adsorption of CO_2 on V_O-$STMn_{0.2}$ than on $STMn_{0.2}$.

The photocatalytic CO_2 reduction performance of the samples was evaluated under xenon lamp illumination in a gas-solid reaction system (Scheme S1 and Fig. 5a). STO showed negligible CO_2 reduction activity, while V_O-STO exhibited a yield of 2.17 µmol g^{-1} CH_4. In sharp contrast, the CO_2 conversion activity of V_O-STM_x was significantly enhanced after reduction with $NaBH_4$. The $STMn_{0.2}$ displayed limited CO_2 photoreduction with 2.07 µmol g^{-1} CO and 1.52 µmol g^{-1} CH_4. In comparison, V_O-$STMn_{0.2}$ yielded 18.21 µmol g^{-1} CH_4 with almost 100 % selectivity for CH_4 production, which demonstrated obvious superiority over the other Mn-doped samples (V_O-$STMn_{0.1}$ 5.20 µmol g^{-1} and V_O-$STMn_{0.3}$ 9.36 µmol g^{-1}, Fig. S10a). Meanwhile, the performance of V_O-$STFe_x$ and V_O-$STCo_x$ were boosted after active surface regulation, whereby the highest CH_4 yields of 7.55 µmol g^{-1} and 11.19 µmol g^{-1} were delivered by V_O-$STFe_{0.3}$ and V_O-$STCo_{0.3}$ (Figs. S11 and S12), respectively. Compared with other single component Ti-based photocatalysts, V_O-STM_x perovskites exhibit excellent CO_2 photoreduction performance under the absence of any co-catalysts and sacrificial reagents (Table S2). Moreover, O_2 evolution was detected in the photocatalytic reaction (Fig. S13). For V_O-$STMn_{0.2}$, the O_2 yield was 35.14 µmol g^{-1}, approximately twice that of CH_4 yield (18.21 µmol g^{-1}). The CH_4/O_2 ratio was close to the theoretical value of 1:2, indicating that photogenerated holes were involved in the oxidation reaction of water to facilitate O_2 evolution.

For further verification, a series of control experiments were carried out, the results of which are shown in Fig. S10b. Negligible photocatalytic products were detected, whether the experiments were carried out in argon, in the dark, without H_2O or without samples. Furthermore, the $^{13}CO_2$ labelling experiment revealed that $^{13}CH_4$ ($m/z = 17$) was the only CO_2 reduction product (Fig. 4b). Almost no H_2 ($m/z = 2$), ^{13}CO ($m/z = 29$) and $^{13}CH_3OH$ ($m/z = 33$) were detected. The results above confirm that the evolution of CH_4 is exclusively originated from the photoreduction of CO_2. Furthermore, surface oxygen vacancies are effective strategies for modulating electronic structure and adjusting surface properties to enhance photocatalytic activity. However, oxygen vacancies are prone to being filled by oxygen molecules or blocked by intermediate species, resulting in a gradual decrease in activity until catalyst deactivation occurs. Therefore, ensuring the stability of defects is a necessary condition for highly efficient and stable photocatalysts [42]. After 15 h of cyclic reactions, the CO_2 reduction performance of V_O-$STMn_{0.2}$ only showed a slight decline compared to the initial state (17.23 vs 18.21 µmol g^{-1}), as seen in Fig. 5c. Corresponding TEM, XRD, Raman, and XPS tests were conducted after 15 h of photocatalysis and are presented in Fig. S14. Considering these results comprehensively, our conclusion is that the loss of surface oxygen induces local lattice mismatch and forms a dense dislocation layer, which is clearly observed in Fig. 2d-e and Fig. S14a. As a result of the regulated coordination state and electronic structure of surface atoms, the dislocation layers can enhance the tolerability of oxygen-containing environments within a certain temperature range, thereby improving the cycle stability of the material [43,44].

3.3. Charge transfer mechanism

To determine the actual effects of transition metal substitution and oxygen vacancy formation, further optical measurements were carried out. The UV-Vis-NIR spectra (Fig. 5d) shows that STO and V_O-STO exhibit the absorption onset at 390 nm, which agrees with the band gap edge absorption of $SrTiO_3$ (3.25 eV), whereas the additional absorption band beyond 600 nm is attributed to the increasing oxygen vacancy

concentration on V_O-STO surface. For $STMn_{0.2}$, due to the doped Mn changing the band gap structure, the band edge position at 480 nm indicates a narrower band gap. The optical response of V_O-$STMn_{0.2}$ was enhanced in the spectrum range of 450–900 nm, which is ascribed to the more abundant oxygen vacancies. Notably, compared to Fig. 5a, the enhancement by visible light absorption cannot be neglected (Fig. S10b, $\geq$ 400 nm). A similar enhanced optical response in the visible light region was also observed in the V_O-$STFe_{0.3}$ and V_O-$STCo_{0.3}$ materials (Fig. S15a). Accordingly, the band gap of V_O-STO, V_O-$STMn_{0.2}$, V_O-$STFe_{0.3}$, and V_O-$STCo_{0.3}$ are calculated to be 3.27, 2.76, 2.85, and 2.83 eV, respectively. The positions of the VB maximum for V_O-STO, V_O-$STMn_{0.2}$, V_O-$STFe_{0.3}$, and V_O-$STCo_{0.3}$ were detected by XPS valence spectra (Fig. S15b). The corresponding standard hydrogen electrode ($E_{VB, NHE}$) can then be calculated via the following formula: $E_{VB, NHE} = \varphi + E_{VB, XPS} - 4.44$, where φ is the work function of the instrument (4.2 eV). Thus, based on those results the electronic band structures versus NHE at pH = 7 can be elucidated and displayed in Fig. 5e. The results show that all the prepared perovskite oxides have suitable band gaps and band edge positions to realize CO_2 reduction and O_2 evolution simultaneously. Furthermore, the apparent quantum efficiency (AQE) for CH_4 evolution was evaluated under the illumination of monochromatic light. As exhibited in Fig. S15c, the AQE response of V_O-$STMn_{0.2}$ matches well to the recorded UV-Vis spectrum, achieving AQE of 0.35 % at 380 nm.

Steady-state photoluminescence (PL) spectroscopy, transient photoluminescent (TSPL) spectroscopy, transient photocurrent (TPC) density and electrochemical impedance spectroscopy (EIS) were executed to probe the efficiency of charge-carrier separation and transportation. As shown by steady-state PL spectra, TPC responses and EIS spectra (Fig. 5f-h), the V_O-$STMn_{0.2}$ has lower PL peak intensity, higher TPC density as well as smaller Nyquist semicircle radius in comparison to the $STMn_{0.2}$. After fitting of the TSPL curves for Fig. 5i, prolonged carrier lifetimes ($\tau_1 = 1.06$ ns; $\tau_2 = 5.99$ ns) were observed for V_O-$STMn_{0.2}$ compared to those for $STMn_{0.2}$ ($\tau_1 = 0.89$ ns; $\tau_2 = 3.34$ ns). In addition, the electronic structures of V_O-$STFe_{0.3}$ and V_O-$STCo_{0.3}$ were further analyzed. As shown in Fig. S16, V_O-$STMn_{0.2}$ has the highest oxygen vacancy content, highest photocurrent density and lowest charge transfer resistance, even when compared to V_O-$STFe_{0.3}$ and V_O-$STCo_{0.3}$. Moreover, the carrier lifetimes (τ_2) of V_O-$STFe_{0.3}$ and V_O-$STCo_{0.3}$ were 4.14 ns and 5.43 ns, respectively, which are lower than that of V_O-$STMn_{0.2}$. This indicates that V_O-$STMn_{0.2}$ has superior optimization effect on the photogenerated carrier separation, since plentiful surface oxygen vacancies act as traps to facilitate the separation of photogenerated carriers [45,46]. These properties lead to a significant improvement in the photocatalytic performance of V_O-$STMn_{0.2}$. It is worth noting that a speak and tail can be observed on the photocurrent curve (Fig. 5g and Fig. S16b). Qualitatively, this phenomenon can be understood as follows. When the light source is turned on, the semiconductor absorbs photons with energies equal to or greater than the bandgap energy, leading to the rapid generation of electron-hole pairs on a picosecond timescale, resulting in an instantaneous increase in photocurrent [47–49]. Over time, the trapping and re-emission processes of photo-generated charge carriers on the traps gradually come into effect, which causes the current to gradually decay to the equilibrium current [50,51]. When the light is turned off, the slow decay of the current can be understood as a result of the gradual re-emission and recombination of charge carriers from the traps, while the negative current is attributed to electrons continuing to move towards the surface to recombine with the remaining holes [52,53].

3.4. Detection of reaction intermediates and CO_2 reduction mechanism

To reveal the mechanism of photocatalytic CO_2 reduction, in situ DRIFTS experiments were carried out on $STMn_{0.2}$ and V_O-$STMn_{0.2}$ under illumination. As for V_O-$STMn_{0.2}$ (Fig. 6a), the new infrared absorption peaks at 1615 cm^{-1} and 1278 cm^{-1} originate from the C=O and O-H stretching of COOH*, respectively, which are regarded as critical

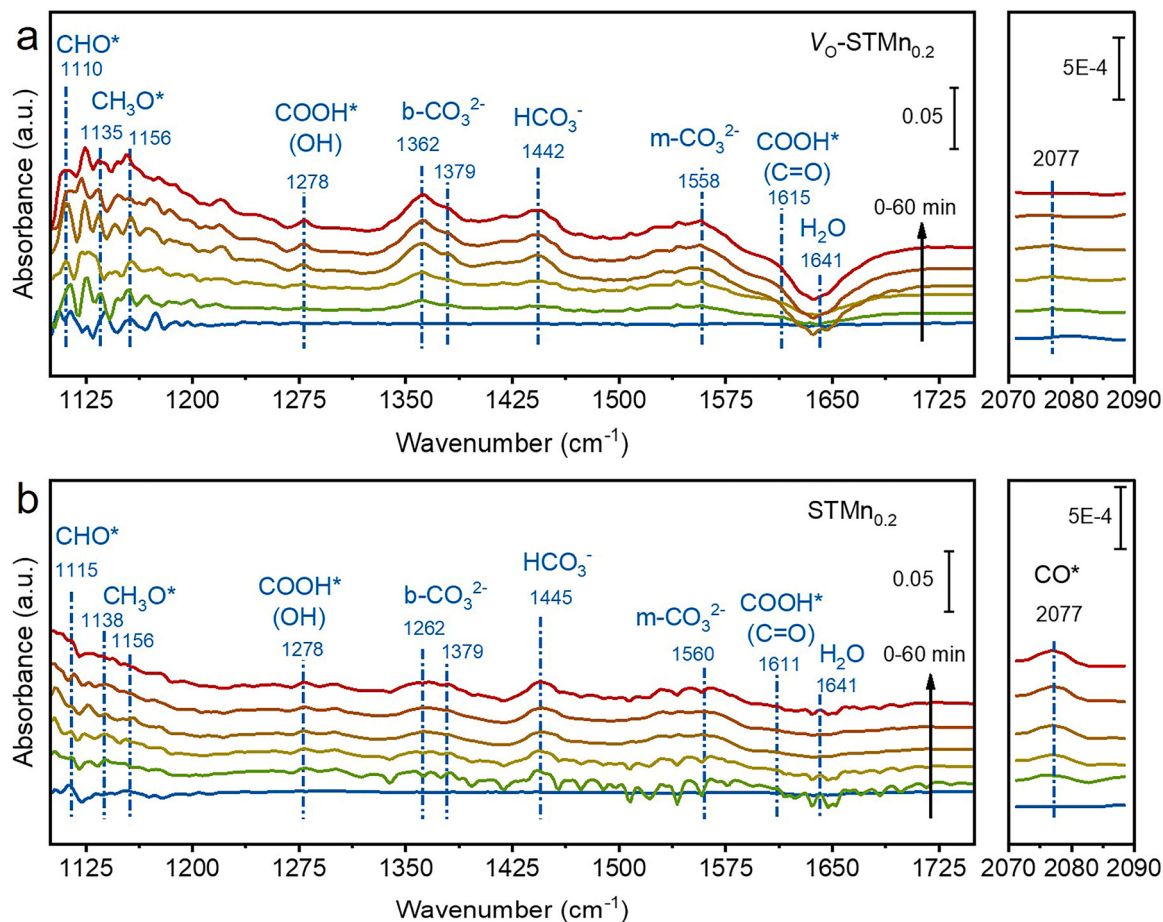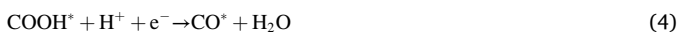**Fig. 6.** In situ DRIFTS test for CO_2 and H_2O interaction with (a) V_O-STMn$_{0.2}$ and (b) STMn$_{0.2}$ under constant Xenon lamp illumination. Amplifications of the areas from 2070 cm^{-1} to 2090 cm^{-1} in (a) and (b), in which the peak at 2077 cm^{-1} corresponds to the adsorbed CO* molecule.

intermediates during the CO_2 conversion to CO or CH_4 [54,55]. The intensity of these peaks then progressively increased with the extension of the illumination time Further, the peak located at 1110 cm^{-1} is associated with the H-C=O bending vibration of the CHO* species, and the peaks at 1135 cm^{-1} and 1156 cm^{-1} can be attributed to the CH_3O^* species [56]. Both CHO* species and CH_3O^* species are important intermediates in the formation of CH_4. Interestingly, the intensity of the observed intermediate species on V_O-STMn$_{0.2}$ was significantly higher than that on STMn$_{0.2}$ (Fig. 6b), further demonstrating the excellent CO_2 methanation activity of V_O-STMn$_{0.2}$. Another drastic distinction between STMn$_{0.2}$ and V_O-STMn$_{0.2}$ arises in the CO* species absorption band at ~2077 cm^{-1}. From the enlarged region (2070–2090 cm^{-1}) of Figs. 6a and 6b, the peak intensity of CO* for STMn$_{0.2}$ increased over the whole time, while for V_O-STMn$_{0.2}$ the peak intensity of CO* showed an initial increase and then gradually decreased [57]. It is indicated that CO* species on the V_O-STMn$_{0.2}$ surface can be rapidly protonated to CHO* and CH_3O^* intermediates instead of being desorbed to form CO molecules, resulting in a nearly 100 % product selectivity for the conversion of CO_2 to CH_4. In this way, the photocatalytic CO_2 reduction processes for different samples could be described as follows:

$$CO_2 + ^* \rightarrow CO_2^* \tag{2}$$

$$CO_2^* + H^+ + e^- \rightarrow COOH^* \tag{3}$$

$$COOH^* + H^+ + e^- \rightarrow CO^* + H_2O \tag{4}$$

$$CO^* \rightarrow ^* + CO\uparrow \text{ or } CO^* + H^+ + e^- \rightarrow CHO^* \tag{5}$$

$$CHO^* + H^+ + e^- \rightarrow CH_2O^* \tag{6}$$

$$CH_2O^* + H^+ + e^- \rightarrow CH_3O^* \tag{7}$$

$$CH_3O^* + H^+ + e^- \rightarrow O^* + CH_4\uparrow \tag{8}$$

$$O^* + H^+ + e^- \rightarrow OH^* \tag{9}$$

$$OH^* + H^+ + e^- \rightarrow ^* + H_2O \tag{10}$$

The Gibbs free energy of the proposed reduction pathway was calculated to investigate the effect of low-coordination transition metal sites on the CO_2 reduction activity (Fig. 7a, Figs. S17 and S18). The overall reaction energy barrier for all oxygen vacancy-containing perovskites is lower than that for oxygen vacancy-free perovskites. The introduction of oxygen vacancies leads to charge enrichment on the low coordination transition metal sites, which allows these metal sites to effectively adsorb and activate the reactants. The desorption of CO* on STM$_x$ is more favorable than the hydrogenation step, thus CO is the major product for STM$_x$. Comparatively, V_O-STM$_x$ preferentially hydrogenates CO*, enabling the selectivity for the CH_4 product close to 100 % (Fig. 4a). Importantly, the rate-determining step (RDS) for all oxygen vacancy-containing perovskites is the desorption of OH* group. The free energy of oxygen-intermediates (CH_2O^*, CH_3O^*, O*, OH*) with the O atom as the center of interaction for V_O-STO, is the most negative of all V_O-STM$_x$ perovskites studied, indicating that the Ti active sites of V_O-STO have the strongest adsorption for these oxygen-intermediates. The RDS barrier of V_O-STM$_x$ is lower than that of V_O-STO, and the limiting barriers of the perovskites V_O-STO, V_O-STMn$_x$, V_O-STFe$_x$ and
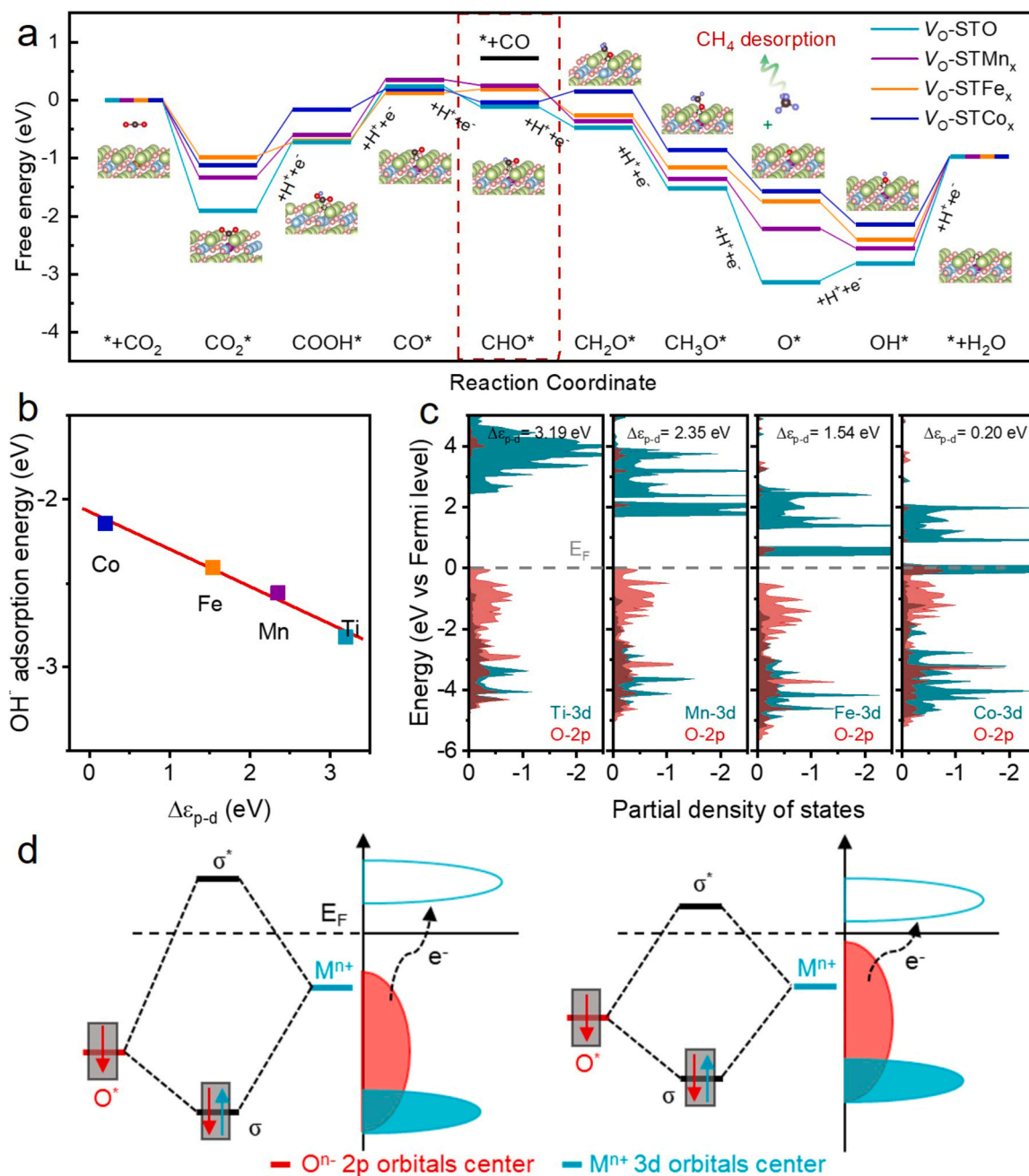
Fig. 7. (a) The Gibbs free energy diagram of CO_2 photoreduction to CH_4 for the perovskites V_O-STO and V_O-STM$_x$. (b) The linear relationship for the adsorption energy of OH* group and the energy difference ($\Delta\varepsilon_{p-d}$) between the O atom 2p band center and the transition metal cation d band center. (c) The partial density of states for the 3d orbitals of transition metal atom and the O 2p orbitals of OH* group. The band centers of spin down were used. (d) Schematic illustration for the hybridization of the d orbital of the metal cation with the oxygen p orbital of the adsorbate with the decrement of $\Delta\varepsilon_{p-d}$.

V_O-STCo$_x$ are 1.84, 1.58, 1.47 and 1.17 eV, respectively, suggesting that the doped transition metal ions weaken the interaction with the oxygen-intermediates.

According to the crystal field effect, the static electric field splits the d orbitals of the MO_6 octahedral metal cation into three low-lying t_{2g} orbitals (d_{xy}, d_{xz}, d_{yz}) and two high-lying e_g orbitals ($d_{x^2-z^2}$, d_{z^2}) [58]. The split d orbitals of the metal cation contribute to the narrow d band. The principle behind the linear relationship for the adsorption energy of the oxygen-intermediates and the energy difference ($\Delta\varepsilon_{p-d}$) between the O atom 2p band center and the metal cation d band center is due to the coupling of the metal cation d orbitals and the O atom 2p orbitals (Figs. 7b and 7c). When low-coordination transition metal cation sites interact with oxygen intermediates, the electrons of transition metal cation d orbitals and 2p orbitals of O atoms spatially overlap, forming σ bonding molecular orbital states and σ* antibonding molecular orbital states (Fig. 7d). As the 2p orbitals center of the O atom approaches or rises above the d orbitals center of the metal cation (smaller $\Delta\varepsilon_{p-d}$), the unbonded electrons of the O atom can transition to the antibonding orbital with relatively less energy. The reduced charge of the O atom and the decreased energy of the antibonding orbitals give the oxygen intermediate a higher degree of freedom [59]. Thus, the Mn atom with a relatively small $\Delta\varepsilon_{p-d}$ may have a more suitable adsorption of oxygen-intermediates, which reduces the unfavorable strong adsorption of oxygen-intermediates and possesses a higher catalytic activity. Another remarkable factor is the influence of the surface oxygen vacancy contents on the CO_2 reduction properties. In fact, when we take

the oxygen vacancy content as a variable, the CO_2 reduction performance is enhanced with the increasing oxygen vacancy concentration and follows a good linear relationship, as illustrated in Fig. S19. However, it should be noted that the catalyst only has the best catalytic activity when the vacancy concentration is at an appropriate level [60].

Briefly, the relative center between the O 2p orbitals and the transition metal 3d orbitals could regulate the adsorption ability of the low-coordination metal cation sites for oxygen-intermediates. Making full use of the parameter $\Delta\varepsilon_{p-d}$, the mechanism of CO_2 reduction reaction for a given STM_x perovskite can be effectively predicted. Meanwhile, the CO_2 reduction performance of strontium titanate-based perovskites also depends on the adsorption properties of other oxygen intermediates (COOH*, CO*, CHO*) during CO_2 reduction, which requires full experimental and theoretical verification in the future.

4. Conclusion

In summary, a model of low-coordination metal active sites was constructed for the tunable selectivity and reactivity of CO_2 photochemical reduction based on strontium titanate perovskites. After activity modification of the STM_x (x = 0.1–0.3) perovskites by reduction with $NaBH_4$, the V_O-$STMn_{0.2}$ exhibited a gas yield of 18.21 µmol g^{-1} with near 100 % selectivity for CH_4. The electronic structure analysis suggest that the introduction of oxygen vacancies leads to charge enrichment on the low-coordination Mn atom. In situ DRIFTS and Gibbs free energy calculations reveal that the charge-rich low-coordination metal sites have lowered the overall activation energy barrier, thus facilitating the hydrogenation of CO* to CH_4. Theoretical calculations demonstrate that the relative centers between the O atom 2p orbitals and the metal 3d orbitals regulate the adsorption properties of the low-coordination metal sites for oxygen-intermediates. In future work, we will carry out a comprehensive study on A-site modulation of perovskites to explore the design options for bifunctional sites photocatalysts with enhanced adsorption properties for COOH*, CO* and CHO* to improve the photocatalytic performance. The results of the study provide insight into the design and defective modulation of photocatalytic materials.

CRediT authorship contribution statement

Yibo Gao: Methodology, Data curation, Formal analysis, Writing – original draft. **Miaomiao Zhang:** Writing – review & editing. **Yang Jin:** Funding acquisition, Writing - review & editing. **Meng Zhou:** Software. **Yanpeng Mao:** Funding acquisition, Conceptualization, Investigation, Resources. **Jian Sun:** Writing – review & editing. **Wenlong Wang:** Resources. **Zhanlong Song:** Resources.

Declaration of Competing Interest

The authors declare that they have no known competing financial interests or personal relationships that could have appeared to influence the work reported in this paper.

Data availability

Data will be made available on request.

Acknowledgements

Appendix A. Supporting information

Supplementary data associated with this article can be found in the online version at doi:10.1016/j.apcatb.2023.123348.

References

[1] S.H. Si, H.W. Shou, Y.Y. Mao, X.L. Bao, G.Y. Zhai, K.P. Song, Z.Y. Wang, P. Wang, Y.Y. Liu, Z.K. Zheng, Y. Dai, L. Song, B.B. Huang, H.F. Cheng, Low-coordination single Au atoms on ultrathin $ZnIn_2S_4$ nanosheets for selective photocatalytic CO_2 reduction towards CH_4, Angew. Chem. Int. Ed. 61 (2022) 10, https://doi.org/10.1002/anie.202209446.

[2] A. Corma, H. Garcia, Photocatalytic reduction of CO_2 for fuel production: possibilities and challenges, J. Catal. 308 (2013) 168–175, https://doi.org/10.1016/j.jcat.2013.06.008.

[3] T. Takata, J.Z. Jiang, Y. Sakata, M. Nakabayashi, N. Shibata, V. Nandal, K. Seki, T. Hisatomi, K. Domen, Photocatalytic water splitting with a quantum efficiency of almost unity, Nature 581 (2020) 411, https://doi.org/10.1038/s41586-020-2278-9.

[4] Q.H. Zhu, Z.H. Xu, B.C. Qiu, M.Y. Xing, J.L. Zhang, Emerging cocatalysts on g-C_3N_4 for photocatalytic hydrogen evolution, Small 17 (2021) 25, https://doi.org/10.1002/smll.202101070.

[5] F. Chen, Z.Y. Ma, L.Q. Ye, T.Y. Ma, T.R. Zhang, Y.H. Zhang, H.W. Huang, Macroscopic spontaneous polarization and surface oxygen vacancies collaboratively boosting CO_2 photoreduction on $BiOIO_3$ single crystals, Adv. Mater. 32 (2020) 8, https://doi.org/10.1002/adma.201908350.

[6] C.Y. Wang, T.Y. Ma, Y.H. Zhang, H.W. Huang, Versatile titanates: classification, property, preparation, and sustainable energy catalysis, Adv. Funct. Mater. 32 (2022) 42, https://doi.org/10.1002/adfm.202107747.

[7] M.M. Zhang, Y.B. Gao, Y.P. Mao, W.L. Wang, J. Sun, Z.L. Song, J. Sun, X.Q. Zhao, Enhanced dry reforming of methane by microwave-mediated confined catalysis over Ni-La/AC catalyst, Chem. Eng. J. 451 (2023) 15, https://doi.org/10.1016/j.cej.2022.138616.

[8] P.V. Balachandran, J. Young, T. Lookman, J.M. Rondinelli, Learning from data to design functional materials without inversion symmetry, Nat. Commun. 8 (2017) 13, https://doi.org/10.1038/ncomms14282.

[9] M. Ezbiri, V. Becattini, M. Hoes, R. Michalsky, A. Steinfeld, High redox capacity of Al-doped $La_{1−x}Sr_xMnO_{3-\delta}$ perovskites for splitting CO_2 and H_2O at Mn-enriched surfaces, ChemSusChem 10 (2017) 1517–1525, https://doi.org/10.1002/cssc.201601869.

[10] B. Choudhury, M. Dey, A. Choudhury, Defect generation, d-d transition, and band gap reduction in Cu-doped TiO_2 nanoparticles, Int. Nano Lett. 3 (2013) 25, https://doi.org/10.1186/2228-5326-3-25.

[11] M.O. Olagunju, X. Poole, P. Blackwelder, M.P. Thomas, B.S. Guiton, D. Shukla, J. L. Cohn, B. Surnar, S. Dhar, E.M. Zahran, L.G. Bachas, M.R. Knecht, Size-controlled $SrTiO_3$ nanoparticles photodecorated with Pd cocatalysts for photocatalytic organic dye degradation, ACS Appl. Nano Mater. 3 (2020) 4904–4912, https://doi.org/10.1021/acsanm.0c01086.

[12] Y.Q. Bi, M.F. Ehsan, Y. Huang, J.R. Jin, T. He, Synthesis of Cr-doped $SrTiO_3$ photocatalyst and its application in visible-light-driven transformation of CO_2 into CH_4, J. CO_2 Util. 13 (2016), https://doi.org/10.1016/j.jcou.2015.11.007.

[13] J.H. Kou, J. Gao, Z.S. Li, H. Yu, Y. Zhou, Z.G. Zou, Construction of visible-light-responsive $SrTiO_3$ with enhanced CO_2 adsorption ability: highly efficient photocatalysts for artifical photosynthesis, Catal. Lett. 145 (2015) 640–646, https://doi.org/10.1007/s10562-014-1415-1.

[14] Q.Y. Wu, J.J. Cen, K.R. Goodman, M.G. White, G. Ramakrishnan, A. Orlov, Understanding the interactions of CO_2 with doped and undoped $SrTiO_3$, ChemSusChem 9 (2016) 1889–1897, https://doi.org/10.1002/cssc.201600498.

[15] S.Y. Wang, K. Teramura, T. Hisatomi, K. Domen, H. Asakura, S. Hosokawa, T. Tanaka, Optimized synthesis of Ag-modified Al-doped $SrTiO_3$ photocatalyst for the conversion of CO_2 using H_2O as an electron donor, ChemistrySelect 5 (2020) 8779–8786, https://doi.org/10.1002/slct.202001693.

[16] L. Pan, H. Mei, G. Zhu, S. Li, X. Xie, S. Gong, H. Liu, Z. Jin, J. Gao, L. Cheng, L. Zhang, Bi selectively doped $SrTiO_{3−x}$ nanosheets enhance photocatalytic CO_2 reduction under visible light, J. Colloid Interface Sci. 611 (2022) 137–148, https://doi.org/10.1016/j.jcis.2021.12.033.

[17] X.C. Jiao, Z.W. Chen, X.D. Li, Y.F. Sun, S. Gao, W.S. Yan, C.M. Wang, Q. Zhang, Y. Lin, Y. Luo, Y. Xie, Defect-mediated electron-hole separation in one-unit-cell $ZnIn_2S_4$ layers for boosted solar-driven CO_2 reduction, J. Am. Chem. Soc. 139 (2017) 7586–7594, https://doi.org/10.1021/jacs.7b02290.

[18] Y.Z. Zhang, X. Zhi, J.R. Harmer, H.L. Xu, K. Davey, J.R. Ran, S.Z. Qiao, Facet-specific active surface regulation of Bi_xMO_y (M=Mo, V, W) nanosheets for boosted photocatalytic CO_2 reduction, Angew. Chem. Int. Ed. 61 (2022) 8, https://doi.org/10.1002/anie.202212355.

[19] J.Y. Zhang, J.M. Qian, J.Q. Ran, P.X. Xi, L.J. Yang, D.Q. Gao, Engineering lower coordination atoms onto NiO/Co_3O_4 heterointerfaces for boosting oxygen evolution reactions, ACS Catal. 10 (2020) 12376–12384, https://doi.org/10.1021/acscatal.0c03756.

[20] Y.H. Cao, L. Guo, M. Dan, D.E. Doronkin, C.Q. Han, Z.Q. Rao, Y. Liu, J. Meng, Z. Huang, K.B. Zheng, P. Chen, F. Dong, Y. Zhou, Modulating electron density of vacancy site by single Au atom for effective CO_2 photoreduction, Nat. Commun. 12 (2021) 10, https://doi.org/10.1038/s41467-021-21925-7.

[21] F. Voigts, C. Argirusis, W. Maus-Friedrichs, The interaction of CO_2 and CO with Fe-doped $SrTiO_3(100)$ surfaces, Surf. Interface Anal. 44 (2012) 301–307, https://doi.org/10.1002/sia.3802.

[22] H. Hirakawa, M. Hashimoto, Y. Shiraishi, T. Hirai, Photocatalytic conversion of nitrogen to ammonia with water on surface oxygen vacancies of titanium dioxide, J. Am. Chem. Soc. 139 (2017) 10929–10936, https://doi.org/10.1021/jacs.7b06634.

[23] Y.X. Zhao, C. Chang, F. Teng, Y.F. Zhao, G.B. Chen, R. Shi, G.I.N. Waterhouse, W. F. Huang, T.R. Zhang, DefecT-engineered Ultrathin Delta-MnO_2 nanosheet arrays as bifunctional electrodes for efficient overall water splitting, Adv. Energy Mater. 7 (2017) 7, https://doi.org/10.1002/aenm.201700005.

[24] H.B. Yang, S.F. Hung, S. Liu, K.D. Yuan, S. Miao, L.P. Zhang, X. Huang, H.Y. Wang, W.Z. Cai, R. Chen, J.J. Gao, X.F. Yang, W. Chen, Y.Q. Huang, H.M. Chen, C.M. Li, T. Zhang, B. Liu, Atomically dispersed Ni(i) as the active site for electrochemical CO_2 reduction, Nat. Energy 3 (2018) 140–147, https://doi.org/10.1038/s41560-017-0078-8.

[25] S. Zhang, Y.X. Zhao, R. Shi, C. Zhou, G.I.N. Waterhouse, L.Z. Wu, C.H. Tung, T. R. Zhang, Efficient photocatalytic nitrogen fixation over $Cu^{δ+}$-modified defective ZnAl-layered double hydroxide nanosheets, Adv. Energy Mater. 10 (2020) 10, https://doi.org/10.1002/aenm.201901973.

[26] D. Li, Y.X. Zhao, Y.X. Miao, C. Zhou, L.P. Zhang, L.Z. Wu, T.R. Zhang, Accelerating electron-transfer dynamics by TiO_2-immobilized reversible single-atom copper for enhanced artificial photosynthesis of urea, Adv. Mater. 34 (2022) 7, https://doi.org/10.1002/adma.202207793.

[27] Y.X. Zhao, Y.F. Zhao, R. Shi, B. Wang, G.I.N. Waterhouse, L.Z. Wu, C.H. Tung, T. R. Zhang, Tuning oxygen vacancies in ultrathin TiO_2 nanosheets to boost photocatalytic nitrogen fixation up to 700 nm, Adv. Mater. 31 (2019) 9, https://doi.org/10.1002/adma.201806482.

[28] K. Xie, N. Umezawa, N. Zhang, P. Reunchan, Y.J. Zhang, J.H. Ye, Self-doped $SrTiO_{3-δ}$ photocatalyst with enhanced activity for artificial photosynthesis under visible light, Energy Environ. Sci. 4 (2011) 4211–4219, https://doi.org/10.1039/c1ee01594j.

[29] B. Wang, S.H. Shen, L.J. Guo, $SrTiO_3$ single crystals enclosed with high-indexed {023} facets and {001} facets for photocatalytic hydrogen and oxygen evolution, Appl. Catal. B Environ. 166 (2015) 320–326, https://doi.org/10.1016/j.apcatb.2014.11.032.

[30] R.D. Shannon, Revised effective ionic radii systematic studies of interatomic distances in halides chalcog, Acta Crystallogr. Sect. A 32 (1976) 751–767, https://doi.org/10.1107/s0567739476001551.

[31] H.J. Yu, J.Y. Li, Y.H. Zhang, S.Q. Yang, K.L. Han, F. Dong, T.Y. Ma, H.W. Huang, Three-in-one oxygen vacancies: whole visible-spectrum absorption, efficient charge separation, and surface site activation for robust CO_2 photoreduction, Angew. Chem. Int. Ed. 58 (2019) 3880–3884, https://doi.org/10.1002/anie.201813967.

[32] G. Ou, Y.S. Xu, B. Wen, R. Lin, B.H. Ge, Y. Tang, Y.W. Liang, C. Yang, K. Huang, D. Zu, R. Yu, W.X. Chen, J. Li, H. Wu, L.M. Liu, Y.D. Li, Tuning defects in oxides at room temperature by lithium reduction, Nat. Commun. 9 (2018) 9, https://doi.org/10.1038/s41467-018-03765-0.

[33] D. Caruntu, T. Rostamzadeh, T. Costanzo, S.S. Parizi, G. Caruntu, Solvothermal synthesis and controlled self-assembly of monodisperse titanium-based perovskite colloidal nanocrystals, Nanoscale 7 (2015) 12955–12969, https://doi.org/10.1039/c5nr00737b.

[34] D. Choudhury, S. Mukherjee, P. Mandal, A. Sundaresan, U.V. Waghmare, S. Bhattacharjee, R. Mathieu, P. Lazor, O. Eriksson, B. Sanyal, P. Nordblad, A. Sharma, S.V. Bhat, O. Karis, D.D. Sarma, Tuning of dielectric properties and magnetism of $SrTiO_3$ by site-specific doping of Mn, Phys. Rev. B 84 (2011), https://doi.org/10.1103/PhysRevB.84.125124.

[35] W.S. Hou, P.L. Feng, X. Guo, Z.H. Wang, Z. Bai, Y. Bai, G.X. Wang, K.N. Sun, Catalytic mechanism of oxygen vacancies in perovskite oxides for lithium-sulfur batteries, Adv. Mater. 34 (2022) 11, https://doi.org/10.1002/adma.202202222.

[36] Q. Zhang, Y. Huang, S.Q. Peng, T.T. Huang, J.J. Cao, W.K. Ho, S. Lee, Synthesis of $SrFe_xTi_{1−x}O_{3-δ}$ nanocubes with tunable oxygen vacancies for selective and efficient photocatalytic NO oxidation, Appl. Catal. B Environ. 239 (2018) 1–9, https://doi.org/10.1016/j.apcatb.2018.07.076.

[37] V.V. Laguta, I.V. Kondakova, I.P. Bykov, M.D. Glinchuk, A. Tkach, P.M. Vilarinho, L. Jastrabik, Electron spin resonance investigation of Mn^{2+} ions and their dynamics in Mn-doped $SrTiO_3$, Phys. Rev. B 76 (2007), https://doi.org/10.1103/PhysRevB.76.054104.

[38] M.Y. Wang, Z.X. Feng, Pitfalls in X-ray absorption spectroscopy analysis and interpretation: a practical guide for general users, Curr. Opin. Electrochem. 30 (2021) 7, https://doi.org/10.1016/j.coelec.2021.100803.

[39] X.D. Li, Y.F. Sun, J.Q. Xu, Y.J. Shao, J. Wu, X.L. Xu, Y. Pan, H.X. Ju, J.F. Zhu, Y. Xie, Selective visible-light-driven photocatalytic CO_2 reduction to CH_4 mediated by atomically thin $CuIn_5S_8$ layers, Nat. Energy 4 (2019) 690–699, https://doi.org/10.1038/s41560-019-0431-1.

[40] J.Q. Xu, Z.Y. Ju, W. Zhang, Y. Pan, J.F. Zhu, J.W. Mao, X.L. Zheng, H.Y. Fu, M. L. Yuan, H. Chen, R.X. Li, Efficient infrared-light-driven CO_2 reduction over ultrathin metallic Ni-doped CoS_2 nanosheets, Angew. Chem. Int. Ed. 60 (2021) 8705–8709, https://doi.org/10.1002/anie.202017041.

[41] H.Y. Gu, X. Liu, X.F. Liu, C.C. Ling, K. Wei, G.M. Zhan, Y.B. Guo, L.Z. Zhang, Adjacent single-atom irons boosting molecular oxygen activation on MnO_2, Nat. Commun. 12 (2021) 9, https://doi.org/10.1038/s41467-021-25726-w.

[42] M.X. Ran, W. Cui, K.L. Li, L.C. Chen, Y.X. Zhang, F. Dong, Y.J. Sun, Light-induced dynamic stability of oxygen vacancies in $BiSbO_4$ for efficient photocatalytic formaldehyde degradation, Energy Environ. Mater. 5 (2022) 305–312, https://doi.org/10.1002/eem2.12176.

[43] L.W. Jiang, Y. Huang, Y. Zou, C. Meng, Y. Xiao, H. Liu, J.J. Wang, Boosting the stability of oxygen vacancies in $α-Co(OH)_2$ nanosheets with coordination polyhedrons as rivets for high-performance alkaline hydrogen evolution electrocatalyst, Adv. Energy Mater. 12 (2022) 9, https://doi.org/10.1002/aenm.202202351.

[44] W.B. Jiang, H.Y. Loh, B.Q.L. Low, H.J. Zhu, J.X. Low, J.Z.X. Heng, K.Y. Tang, Z. B. Li, X.J. Loh, E.Y. Ye, Y.J. Xiong, Role of oxygen vacancy in metal oxides for photocatalytic CO_2 reduction, Appl. Catal. B Environ. 321 (2023) 22, https://doi.org/10.1016/j.apcatb.2022.122079.

[45] Y. Shen, C.J. Ren, L.R. Zheng, X.Y. Xu, R. Long, W.Q. Zhang, Y. Yang, Y.C. Zhang, Y.F. Yao, H.Q. Chi, J.L. Wang, Q. Shen, Y.J. Xiong, Z.G. Zou, Y. Zhou, Room-temperature photosynthesis of propane from CO_2 with Cu single atoms on vacancy-rich TiO_2, Nat. Commun. 14 (2023) 9, https://doi.org/10.1038/s41467-023-36778-5.

[46] Y.H. Huang, K. Wang, T. Guo, J. Li, X.Y. Wu, G.K. Zhang, Construction of 2D/2D $Bi_2Se_3/g-C_3N_4$ nanocomposite with High interfacial charge separation and photo-heat conversion efficiency for selective photocatalytic CO_2 reduction, Appl. Catal. B Environ. 277 (2020) 9, https://doi.org/10.1016/j.apcatb.2020.119232.

[47] B. Chen, P.N. Rudd, S. Yang, Y.B. Yuan, J.S. Huang, Imperfections and their passivation in halide perovskite solar cells, Chem. Soc. Rev. 48 (2019) 3842–3867, https://doi.org/10.1039/c8cs00853a.

[48] L.M. Peter, Energetics and kinetics of light-driven oxygen evolution at semiconductor electrodes: the example of hematite, J. Solid State Electrochem. 17 (2013) 315–326, https://doi.org/10.1007/s10008-012-1957-3.

[49] Z. Li, W.Y. Wang, N.C. Greenham, C.R. McNeill, Influence of nanoparticle shape on charge transport and recombination in polymer/nanocrystal solar cells, Phys. Chem. Chem. Phys. 16 (2014) 25684–25693, https://doi.org/10.1039/c4cp01111b.

[50] Z. Li, F. Gao, N.C. Greenham, C.R. McNeill, Comparison of the operation of polymer/fullerene, polymer/polymer, and polymer/nanocrystal solar cells: a transient photocurrent and photovoltage study, Adv. Funct. Mater. 21 (2011) 1419–1431, https://doi.org/10.1002/adfm.201002154.

[51] Y.M. Ma, S.R. Pendlebury, A. Reynal, F. Le Formal, J.R. Durrant, Dynamics of photogenerated holes in undoped $BiVO_4$ photoanodes for solar water oxidation, Chem. Sci. 5 (2014) 2964–2973, https://doi.org/10.1039/c4sc00469h.

[52] P. Basumatary, P. Agarwal, Photocurrent transient measurements in $MAPbI_3$ thin films, J. Mater. Sci. -Mater. Electron. 31 (2020) 10047–10054, https://doi.org/10.1007/s10854-020-03549-7.

[53] R.A. Belisle, W.H. Nguyen, A.R. Bowring, P. Calado, X. Li, S.J.C. Irvine, M. D. McGehee, P.R.F. Barnes, B.C. O'Regan, Interpretation of inverted photocurrent transients in organic lead halide perovskite solar cells: proof of the field screening by mobile ions and determination of the space charge layer widths, Energy Environ. Sci. 10 (2017) 192–204, https://doi.org/10.1039/c6ee02914k.

[54] X.Y. Jiang, J.D. Huang, Z.H. Bi, W.J. Ni, G. Gurzadyan, Y.A. Zhu, Z.Y. Zhang, Plasmonic active "Hot Spots"-confined photocatalytic CO_2 reduction with high selectivity for CH_4 production, Adv. Mater. 34 (2022) 12, https://doi.org/10.1002/adma.202109330.

[55] L.S. Jiang, J. Li, Y. Li, X.Y. Wu, G.K. Zhang, Promoted charge separation from nickel intervening in $Bi_2O_2^{2+}$ layers of Bi_2O_2S crystals for enhanced photocatalytic CO_2 conversion, Appl. Catal. B Environ. 294 (2021) 10, https://doi.org/10.1016/j.apcatb.2021.120249.

[56] P.G. Liu, Z.X. Huang, X.P. Gao, X. Hong, J.F. Zhu, G.M. Wang, Y.E. Wu, J. Zeng, X. S. Zheng, Synergy between palladium single atoms and nanoparticles via hydrogen spillover for enhancing CO_2 photoreduction to CH_4, Adv. Mater. 34 (2022) 11, https://doi.org/10.1002/adma.202200057.

[57] J. Li, H.L. Huang, W.J. Xue, K. Sun, X.H. Song, C.R. Wu, L. Nie, Y. Li, C.Y. Liu, Y. Pan, H.L. Jiang, D.H. Mei, C.L. Zhong, Self-adaptive dual-metal-site pairs in metal-organic frameworks for selective CO2 photoreduction to CH4, Nat. Catal., 5 (2022) 463–463. https://doi.org/10.1038/s41929-022-00805-3.

[58] Y.M. Sun, H.B. Liao, J.R. Wang, B. Chen, S.N. Sun, S.J.H. Ong, S.B. Xi, C.Z. Diao, Y. H. Du, J.O. Wang, M.B.H. Breese, S.Z. Li, H. Zhang, Z.C.J. Xu, Covalency competition dominates the water oxidation structure-activity relationship on spinel oxides, Nat. Catal. 3 (2020) 554–563, https://doi.org/10.1038/s41929-020-0465-6.

[59] X.P. Wang, S.B. Xi, P.R. Huang, Y.H. Du, H.Y. Zhong, Q. Wang, A. Borgna, Y. W. Zhang, Z.B. Wang, H. Wang, Z.G. Yu, W.S.V. Lee, J.M. Xue, Pivotal role of reversible NiO_6 geometric conversion in oxygen evolution, Nature 611 (2022) 702, https://doi.org/10.1038/s41586-022-05296-7.

[60] C. Xie, D.F. Yan, H. Li, S.Q. Du, W. Chen, Y.Y. Wang, Y.Q. Zou, R. Chen, S.Y. Wang, Defect chemistry in heterogeneous catalysis: recognition, understanding, and utilization, ACS Catal. 10 (2020) 11082–11098, https://doi.org/10.1021/acscatal.0c03034.